Preparation of thin-walled $Na_2Ti_3O_7$ nanotube and its electrochemical properties

Mingzhen Ding[1], Jia Cheng[2], Zhouzhou Li[1], Ying Chen[1], Ke Zhang[1], Jie Qu[1,]*

[1]College of Chemistry and Chemical Engineering, Hunan Normal University, Changsha 410081, China
[2] Hunan Hua Teng Pharmaceutical Co., Ltd, Changsha 410205, P. R. China
[*]E-mail: qujie@hunnu.edu.cn

Sodium-ion battery is one of the most promising alternatives to lithium-ion devices. However, suitable anode materials still need further research. Here, $Na_2Ti_3O_7$ (NTO) nanotubes were synthesized by a facile one-step hydrothermal method, and the morphology was controlled by varying the hydrothermal temperature. X-ray diffraction (XRD) and Transmission electron microscopy (TEM) studies are performed to investigate the morphology and structure of the prepared samples. The results show that NTO-150 owns only 2-3 walls with a thickness of ca. 4 nm. Cyclic voltammetry (CV) and galvanostatic cycling demonstrate that NTO-150 owns higher specific capacity and better cycling stability. Electrochemical impedance spectroscopy (EIS) further indicates such nanotubes with thin wall thickness, tubular structure and large volume space can not only promote the ion transport kinetics, but also accommodate the volume expansion.

1. INTRODUCTION

Sodium-ion battery (SIB) has recently attracted great interest due to the advantage of it's high natural abundance and broad distribution on the earth compared with lithium, which has been selected as one of the most potential candidates for the next generation of large-scale stationary applications [1-3]. However, the large radius of Na^+ ion (1.02 Å) makes it difficult to insert into the electrode materials, thus the current research on SIBs is primarily focused on electrode materials (cathode and anode materials) [4, 5]. Up to now, a host of cathode materials, including NASICON-type [6, 7], $Na_3V_2(PO_4)_3$ [8], Na_2FePO_4F [9], Prussian blue [10] and so on [11-14], have been identified to present excellent capacity, while anode materials with outstanding electrochemical performance still need further studying.

As is well known, carbon-based materials are commonly used as anode in LIBs, but not effectively used for SIBs [15, 16]. For example, graphite, the anode choice for LIBs, shows worse electrochemical activities in SIBs, because it is difficult for Na^+'s insertion [17]. Hard carbon can accommodate the insertion due to its large interlayer space and nanopores, however such storage occurs close to the sodium-plating voltage, raising potential safety concerns [16].

Other potential materials are also being explored, such as metal sulfides [18, 19], metal oxides [20-22], and et al [23, 24]. $Na_2Ti_3O_7$ (NTO) is one of the proper choices due to its lower sodiation/desodiation voltage (with a plateau centered at 0.3 V vs. Na/Na^+) and high specific capacity (~177 mAh g^{-1}) [25, 26]. Obviously, the morphology of the material also shows great influence on the property of the corresponded battery. Nanotubes with large surface area and open tunnel structure indicate superior electrochemical performance due to their specific geometric characteristics. Such structure can also accommodate the volume change during the cycling. Herein, a facile one-step hydrothermal method was used to synthesize NTO nanotubes with large surface area, which can provide more locations for sodium ions to insert. Furthermore, NTO owns a unique zigzag layer structure constructed by titanium and oxygen octahedrons, which can facilitate the transport of Na^+ ions in the interlayer space [27, 28]. Excellent capacity and cycling stability after a gradual activation process were obtained.

2. EXPERIMENTS

2.1. Synthesis of $Na_2Ti_3O_7$ materials

NTO-130: First, a-TiO_2 powder (3 g) was added to an aqueous solution of NaOH (10 M, 80 mL) in a beaker. After sonicating in an ultrasonic bath for 0.5 h, the resulting suspension was transferred to a Teflon-lined autoclave and heated at 130°C for 48 h. The white product was collected and rinsed with deionized water until the pH value of ~7. NTO nanotubes were obtained after drying at 60 °C for 24 h in a conventional oven.

NTO-150: It was synthesized in a similar route, by changing the hydrothermal temperature to 150 °C.

2.2. Structural analysis

Power X-ray diffraction (XRD) was performed on an APEX II DUO diffractometer operated in transmission mode with Mo Cu radiation source (λ=1.54056Å). Transmission electron microscopy (TEM) was performed on JEOL JEM-2100. Brunauere-Emmett-Teller (BET) measurements to measure the surface areas of the as-prepared samples were carried out using a ASAP2010C instrument, using nitrogen as the working gas.

2.3. Preparation of the electrodes

The powder of obtained active materials (70%) was mixed with 20% super conductive black as the conductive agent and 10% polyvinylidene fluoride (PVDF) as the binder in an appropriate amount of 1-methyl-2-pyrrolidinone (NMP). The mixed viscous slurry was pasted onto a copper with a subsequent drying a 105°C for 12 h in vacuum. The resulting foil was roll-pressed and cut into disks (Dia. 8 mm) as working electrodes. All electrochemical analyses were conducted by using two-electrode Swagelok cells, in which a piece of sodium metal was used as the counter and reference electrode, a glass fiber (Whatman GF/D) as the separator. The electrolyte was composed of 1 M $NaClO_4$ dissolved in ethylene carbonate (EC) and diethyl carbonate (DEC) at a weight ratio of 1:1. The cycling performance was performed over a voltage of 0.01-2.5 V (vs. Na/Na^+) at 1 C current density on LAND (WuHan Kingnuo Electronic co. China). The cyclic voltammetry (CV) measurements were performed on a CHI660C with a scan rate of 0.1 mV s^{-1} and different scan rates in a voltage range of 0.01-2.5 V (vs. Na/Na^+). The electrochemical impedance spectroscopy (EIS) was conducted on Zahner electrochemical workstation (Zahner Ennium Co., Germany) with a frequency range from 100 KHz to 0.1 Hz.

3. RESULTS AND DISCUSSION
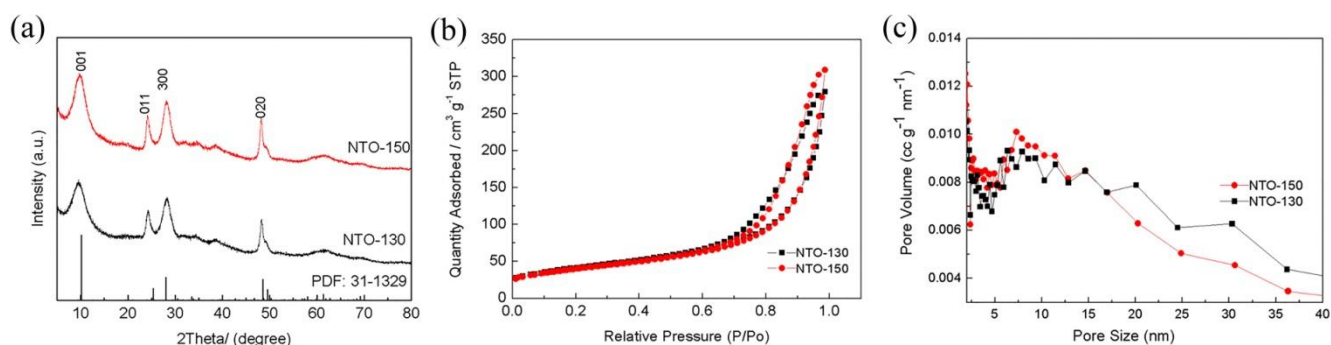
Figure 1. (a) X-ray diffraction (XRD) patterns of NTO-130 and NTO-150 with Mo Cu as the radiation source (λ=1.54056Å), (b) N_2 adsorption-desorption isotherms and (c) pore size distribution curves of NTO-150 and NTO-130.

The XRD patterns of the as-prepared NTO-130 and NTO-150 are showed in Figure 1(a). All of the diffraction peaks can be indexed to the monoclinic NTO phase (JCPDS No. 31-1329) with a P21/m space group. Obviously, no impurity phases were observed in the diffraction, indicating the high purity of the samples. Monoclinic phase owns a special crystal structure, in which three edges shared TiO_6 octahedrons are arranged in a zigzag pattern, and Na^+ ions are inserted in the TiO_6 layers. Such structure can facilitate the transport of Na^+ ions [28].

The specific surface area and pore size distribution of NTO-150 and NTO-130 samples were studied using N_2 adsorption-desorption isothermal characterization. As shown in Figure 1(b), the N_2

adsorption-desorption isothermal curves for both samples are of type IV [29], which is typical of mesoporous materials [17]. And from the pore size distribution curves shown in Figure 1(c), the average pore size of both samples is in the range of 3-15 nm, indicating the existence of mesopores. The specific surface areas of NTO-130 and NTO-150 are 110.78 and 140.5 $m^2 g^{-1}$, respectively. Such large specific surface areas are benefit for more sodium ions' insertion, which can effectively improve the specific capacity of SIBs.
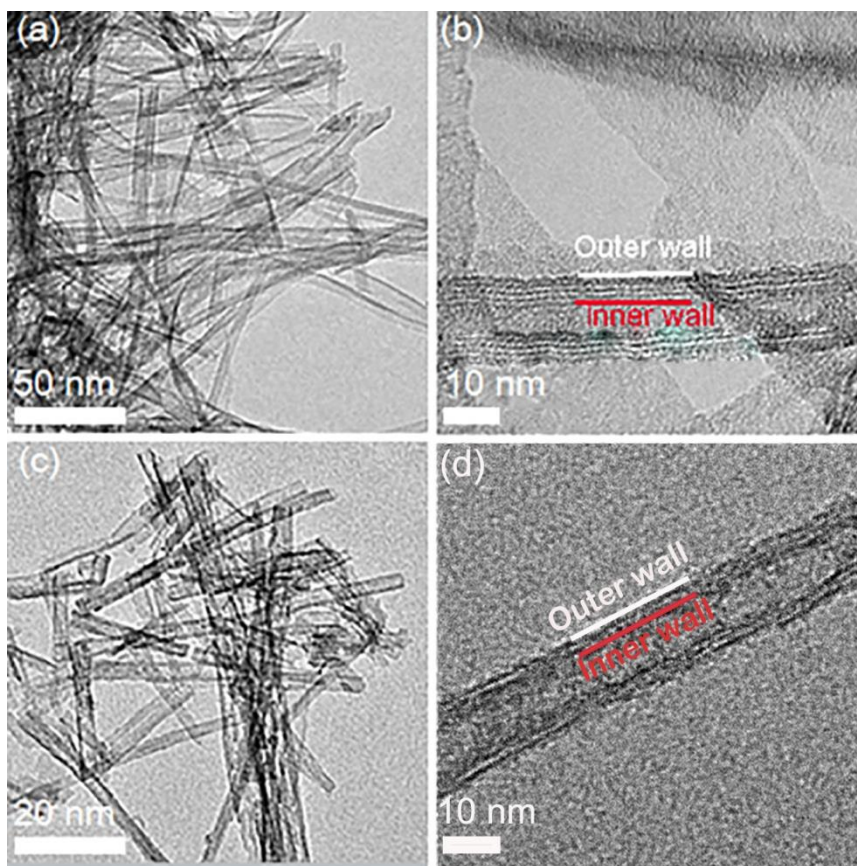

Figure 2. (a) TEM image and (b) HRTEM image of NTO-130; (c) TEM image and (d) HRTEM image of NTO-150.

To further explore the morphology and microstructure, transmission electron microscopy (TEM) and high-resolution TEM (HRTEM) were carried out. As shown in Figure 2(a) and 2(c), both of the NTO-150 and NTO-130 possess a distinct tubular structure. The morphology of the samples altered with the hydrothermal reaction temperature changing. When the reaction temperature is 130 °C, the nanotube is composed of 4-6 walls with the outer diameter of ca. 18 nm and the inner diameter of ca. 6 nm (Figure 2(b)). After the temperature raising to 150 °C, the number of walls obviously reduces to 2-3. The outer and inner diameters of the nanotube are ca. 16 nm and 8 nm, respectively (Figure 2(d)). It is clear that the wall thickness of 150 °C nanotube (ca. 4 nm) is much thinner than 130 °C (ca. 6 nm), for which the thinner wall thickness could shorten the transfer distance of Na^+ ions. On the

other hand, the large volume space of the nanotubes can well alleviate the volume expansion during sodiation, which may reduce the drastic capacity loss in the charge/discharge process.
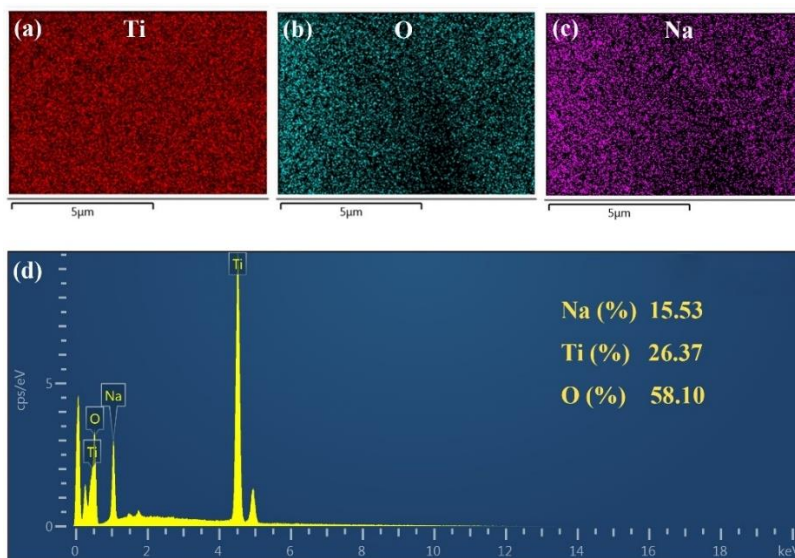

Figure 3. Elemental mappings of Ti (a), O (b) and Na (c); (d) EDS spectrum of NTO-150.
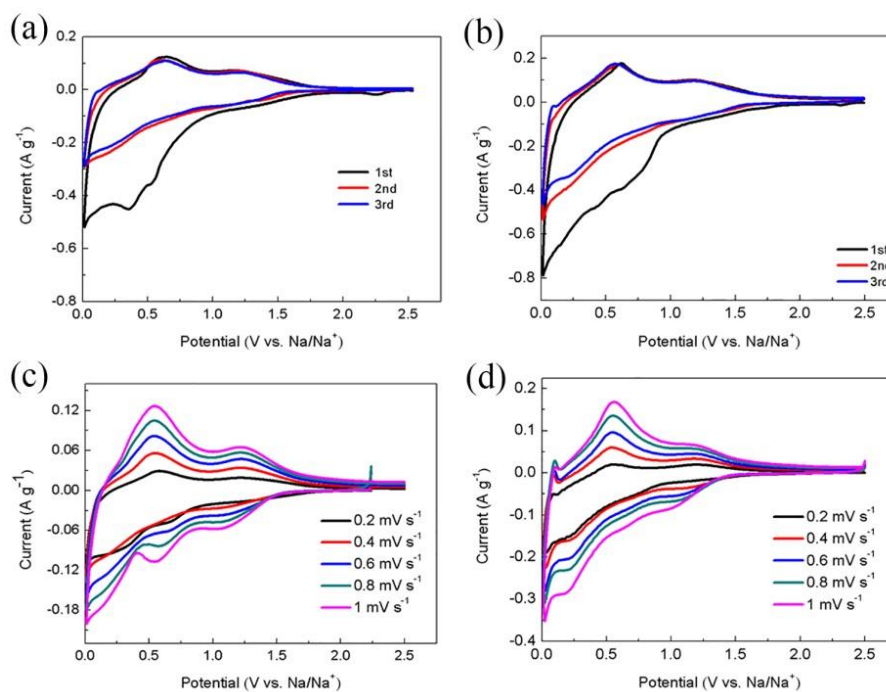
Figure 4. CV curves of (a) NTO-130 and (b) NTO-150 in the initial three cycles at a scan rate of 0.1 mV s^{-1} over a voltage range of 0.01-2.5V; CV curves of (c) NTO-130 and (d) NTO-150 at various scan rates of 0.2, 0.4, 0.6, 0.8, 1 mV s^{-1}, respectively.

The relative elemental mappings of Ti, O and Na for NTO-150 sample are displayed in Figure 3(a), 3(b) and 3(c), respectively. It can be clearly seen that the three elements are uniformly distributed in the sample. Figure 3(d) shows the EDS spectrum of NTO-150 with analytical results inserted. The atomic ratio of Na:Ti:O is 2:3.4:7.6, corresponding to $Na_2Ti_3O_7$, which is consistent with XRD result.

Figure 4(a) and 4(b) shows the cyclic voltammetry (CV) curves of NTO-130 and NTO-150 for the initial three cycles at a scanning rate of 0.1 mV s^{-1} in a voltage range of 0.01-2.5 V. In the first cathodic cycle of the NTO-130 electrode, two reductive peaks at 0.52 and 0.36 V were observed, which might be ascribed to the formation of a solid electrolyte interface (SEI) film [30]. A broad peak around 0.77 V was detected for NTO-150, which corresponds to the decomposition reaction of the electrolyte during the formation of the SEI layer [31]. And all these peaks disappeared in the next two cycles. In the anodic process, the prominent peak of the two samples appeared at about 0.6 V is related to the reversible extraction of Na^+ and oxidation process of Ti^{3+} to Ti^{4+} [32]. Moreover, there is also a broad peak at around 1.13 V, which is caused by the incomplete oxidation of Ti^{3+} [33]. In subsequent cycling, the CV curves were almost coincident, indicating that both electrodes have excellent reversibility and stable Na^+ ion sodiation/desodiation processes. To further investigate the electrochemical processes of the electrodes, the study of CV curves was carried out at various scan rates between 0.2 and 1 mV s^{-1}. As shown in Figures 4(c) and 4(d), all the roughly shapes of the CV curves are almost identical at different scan rates. The intensity of charge and discharge currents increase with the scan rate across the entire potential window. The slight peak potential shifts in both samples implies that no serious electrode polarization was occurred in the charge/discharge reaction.
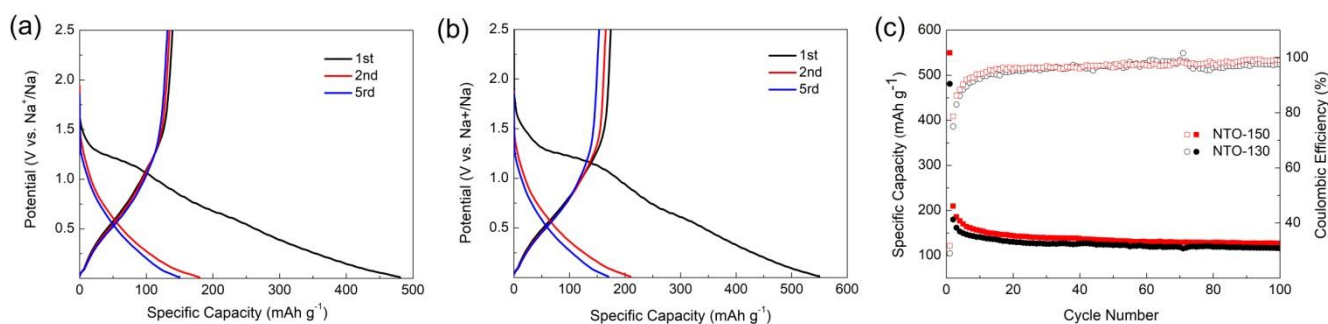
Figure 5. The galvanostatic charge/discharge profiles of (a) NTO-130 and (b) NTO-150 for the 1st, 2nd, 5rd cycles; (c) discharge specific capacity and Coulombic efficiencies of NTO-130 and NTO-150 electrodes at a current density of 1 C (1 C=178 mA g^{-1}).

The galvanostatic charge/discharge profiles of NTO-130 and NTO-150 electrodes at 0.1 C between 0.01-2.5 V are showed in Figure 5(a) and 5(b). The profiles exhibit the typical electrochemical characteristics of the sodiation/desodiation process in NTO materials [29]. The major irreversible capacity in the voltage range of 1.25-1.0 V during the first discharge process is corresponded to the formation of the SEI film on the electrode surface accompanied by electrolyte decomposition [29]. And in the voltage range of 1.0-0.01V, the discharge curve shows an oblique line, indicating that Na$^+$

ions were inserted into the host structure of the as-prepared NTO electrode. The NTO-150 electrode delivers a high initial discharge specific capacity of 549.7 mAh g^{-1}, much higher than the NTO-130 (480.9 mAh g^{-1}). An obvious irreversible capacity is observed for both samples because of the formation of SEI films, which is consistent with the CV results. It is worth noticing that the Coulombic efficiency is significantly improved after the initial cycles (5(c)). The value of NTO-150 is close to 100%, demonstrating a good cyclic stability. The comparison of the electrochemical properties with NTO materials is showed in Table 1. It is clear that after 100 cycles the NTO nanotube prepared in this study possesses an excellent capacity of 127.1 mAh g^{-1}, which is much higher than most of the materials reported in the literature. Such results may due to the thinner wall and hollow tubular structure of prepared NTO nanotubes.

Table 1. Electrochemical performance of $Na_2Ti_3O_7$ materials for sodium ion batteries in previous reports and present work.

Morphology	Thickness/ diameter	Current density [mA g^{-1}]	Cycle number	Specific capacity [mAh g^{-1}]	Reference
Nanotubes	20-30 nm	400	100	200	[34]
Nanosheets	1.2 nm	500	300	110	[35]
Microspheres	2–3 μm	400	120	80.7	[36]
Nanotubes	1 nm	354	100	108	[28]
Nanosheets	5 nm	100	500	108.7	[29]
Nanorods	1–2 μm	100	800	34	[32]
Nanotubes	4 nm	178	100	127.1	This work

Note: For microspheres, the values denote the diameter.
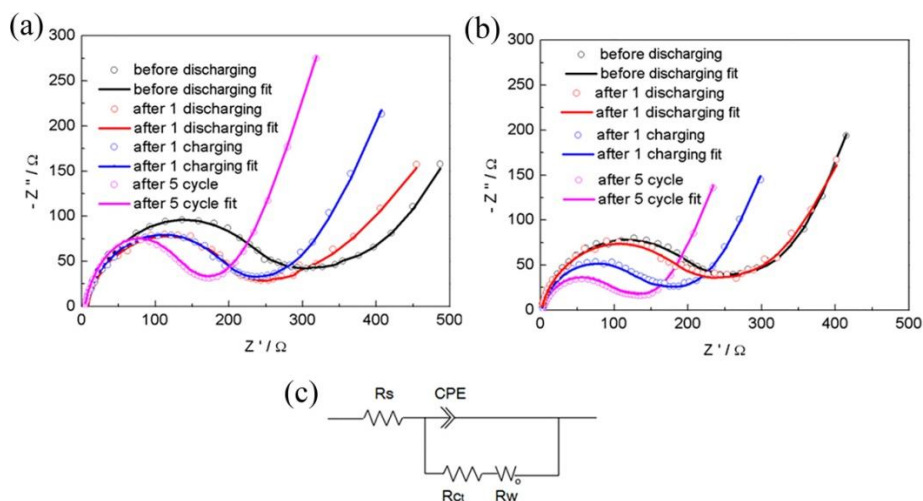
Figure 6. Nyquist plots and the electrochemical fit results of (a) NTO-130 and (b) NTO-150 electrodes before and after different cycles in the frequency range from 100 KHz to 0.1 Hz; (c) the equivalent circuit diagram.

Int. J. Electrochem. Sci., 16 **(2021)** Article ID: 21059

8

Table 2. Circuit analysis results of NTO-130 and NTO-150 samples.

Materials		Before cycle	After 1 discharge	After 1 charge	After 5 cycle
NTO-130	R_{ct} (Ω)	300.9	260.3	233.5	178.5
	R_w (Ω)	310.5	265.5	232.5	165.5
NTO-150	R_{ct} (Ω)	220.5	205.5	145.7	102.9
	R_w (Ω)	215.4	216.9	150.6	99.7

Figure 6(a) and 6(b) depict the electrochemical impedance spectroscopy (EIS) of NTO-130 and NTO-150. The two materials show similar Nyquist diagram, semicircle in the mid-high frequency region and linear slope in the low frequency region. The EIS data were fitted with an equivalent circuit as shown in Figure 6(c). R_{ct} and R_w represent the charge transfer impedance and diffusion resistance, respectively [37]. The fitting values are presented in Table 2, the R_{ct} value of NTO-130 was 300.9 Ω and the value of NTO-150 was 220.5 Ω before cycle. After the initial activation cycles, the values for both of the two samples decrease with the cycling. Before cycling, the samples own high surface energy which could result in a high interfacial impedance. After cycling, the generated SEI film covers on the surface of the sample, reducing the surface energy of the adsorbed Na^+ ions, which decreases the interfacial impedance. It is noteworthy that both of the R_{ct} and R_w values of NTO-150 are much lower than NTO-130, which may due to the thinner wall of the NTO-150. It is much easier for Na^+ ions' transfer, rendering a better cycling performance.

4. CONCLUSIONS

In summary, $Na_2Ti_3O_7$ nanotubes are prepared under alkaline environment using a simple hydrothermal method. The prepared NTO-150 sample owns a thin wall thickness of ca. 4 nm with only 2-3 walls and large specific surface area of 140.5 m^2 g^{-1}. Electrochemical test results indicate that the NTO-150 electrode can maintain a discharge capacity of 127.1 mAh g^{-1} after 100 cycles at a current density of 1 C, and the Coulombic efficiency is close to 100% over the entire cycle range. Such excellent result is mainly due to the thin wall and tubular structure of NTO-150, which can facilitate the insertion of Na^+ ions and promote the ion transport kinetics. Furthermore, NTO-150 with the larger volume space can better accommodate the volume expansion during charging and discharging process and reduce the capacity loss, resulting in excellent electrochemical performance. All of the results reveal that NTO-150 with thinner wall and tubular structure have the potential to be widely used in SIBs.

References

1. H. Kim, H. Kim, Z. Ding, M. H. Lee, K. Lim, G. Yoon and K. Kang, *Advanced Energy Materials*, 6 (2016) 1600943.
2. M. D. Slater, D. Kim, E. Lee and C. S. Johnson, *Advanced Functional Materials*, 23 (2013) 947.
3. N. Yabuuchi, K. Kubota, M. Dahbi and S. Komaba, *Chemical Reviews*, 114 (2014) 11636.
4. L. Gao, L. Wang, S. Dai, M. Cao, Z. Zhong, Y. Shen and M. Wang, *Journal of Power Sources*, 344 (2017) 223.
5. Y. Xu, M. Zhou and Y. Lei, *Advanced Energy Materials*, 6 (2016) 1502514.
6. S. Chen, C. Wu, L. Shen, C. Zhu, Y. Huang, K. Xi, J. Maier and Y. Yu, *Advanced Materials*, 29 (2017) 1700431.
7. Q. Sun, Q.-Q. Ren and Z.-W. Fu, *Electrochemistry Communications*, 23 (2012) 145.
8. Z. Jian, L. Zhao, H. Pan, Y.-S. Hu, H. Li, W. Chen and L. Chen, *Electrochemistry Communications*, 14 (2012) 86.
9. B. L. Ellis, W. R. M. Makahnouk, W. N. Rowan-Weetaluktuk, D. H. Ryan and L. F. Nazar, *Chemistry of Materials*, 22 (2010) 1059.
10. Y. Lu, L. Wang, J. Cheng and J. B. Goodenough, *Chemical Communications*, 48 (2012) 6544.
11. X. Cao, J. Zhou, A. Pan and S. Liang, *Acta Physico-Chimica Sinica*, 36 (2020) 1905018.
12. B.-C. Jang, S.-B. Yang and J.-T. Son, *Journal of Nanoscience and Nanotechnology*, 16 (2016) 8347.
13. D. Su, H.-J. Ahn and G. Wang, *Npg Asia Materials*, 5 (2013) e70.
14. Y. You and A. Manthiram, *Advanced Energy Materials*, 8 (2018) 1701785.
15. M.-S. Balogun, Y. Luo, W. Qiu, P. Liu and Y. Tong, *Carbon*, 98 (2016) 162.
16. Y. Kim, K.-H. Ha, S. M. Oh and K. T. Lee, *Chemistry-a European Journal*, 20 (2014) 11980.
17. M. M. Leite, V. L. Martins, F. M. Vichi and R. M. Torresi, *Electrochimica Acta*, 331 (2020) 135422.
18. Y. Xiao, S. H. Lee and Y.-K. Sun, *Advanced Energy Materials*, 7 (2017) 1601329.
19. H. Song, A. Tang, G. Xu, L. Liu, M. Yin and Y. Pan, *International Journal of Electrochemical Science*, 13 (2018) 4720.
20. J. Qin, N. Zhao, C. Shi, E. Liu, F. He, L. Ma, Q. Li, J. Li and C. He, *Journal of Materials Chemistry A*, 5 (2017) 10946.
21. P. C. Rath, J. Patra, D. Saikia, M. Mishra, J.-K. Chang and H.-M. Kao, *Journal of Materials Chemistry A*, 4 (2016) 14222.
22. L. Wang, X. Bi and S. Yang, *Advanced Materials*, 28 (2016) 7672.
23. H. Kang, Y. Liu, K. Cao, Y. Zhao, L. Jiao, Y. Wang and H. Yuan, *Journal of Materials Chemistry A*, 3 (2015) 17899.
24. K. Kubota and S. Komaba, *Journal of the Electrochemical Society*, 162 (2015) A2538.
25. G. Rousse, M. Elena Arroyo-de Domablo, P. Senguttuvan, A. Ponrouch, J.-M. Tarascon and M. Rosa Palacin, *Chemistry of Materials*, 25 (2013) 4946.
26. P. Senguttuvan, G. Rousse, V. Seznec, J.-M. Tarascon and M. Rosa Palacin, *Chemistry of Materials*, 23 (2011) 4109.
27. J. Nava-Avendano, A. Morales-Garcia, A. Ponrouch, G. Rousse, C. Frontera, P. Senguttuvan, J. M. Tarascon, M. E. Arroyo-de Dompablo and M. R. Palacin, *Journal of Materials Chemistry A*, 3 (2015) 22280.
28. W. Wang, C. Yu, Z. Lin, J. Hou, H. Zhu and S. Jiao, *Nanoscale*, 5 (2013) 594.
29. S. Anwer, Y. Huang, J. Liu, J. Liu, M. Xu, Z. Wang, R. Chen, J. Zhang and F. Wu, *Acs Applied*

Materials & Interfaces, 9 (2017) 11669.
30. Z. Li, Y. Huang, Y. Jiang, Z. Wang, B. Lu, J. Zhou and M. Xie, *Chemelectrochem*, 7 (2020) 2258.
31. M. Zarrabeitia, F. Nobili, M. Angel Munoz-Marquez, T. Rojo and M. Casas-Cabanas, *Journal of Power Sources*, 330 (2016) 78.
32. Z. Chen, L. Lu, Y. Gao, Q. Zhang, C. Zhang, C. Sun and X. Chen, *Materials*, 11 (2018) 2206.
33. D. Kong, Y. Wang, S. Huang, Y. Von Lim, J. Zhang, L. Sun, B. Liu, T. Chen, P. Valdivia y Alvarado and H. Y. Yang, *Journal of Materials Chemistry A*, 7 (2019) 12751.
34. Y. Zhang, L. Guo and S. Yang, *Chemical Communications*, 50 (2014) 14029.
35. J. S. Ko, V. V. T. Doan-Nguyen, H.-S. Kim, G. A. Muller, A. C. Serino, P. S. Weiss and B. S. Dunn, *Acs Applied Materials & Interfaces*, 9 (2017) 1416.
36. S. Chen, L. Gao, L. Zhang and X. Yang, *Ionics*, 25 (2019) 2211.
37. L. Gao, D. Huang, Y. Shen and M. Wang, *Journal of Materials Chemistry A*, 3 (2015) 23570